RSC Advances

ROYAL SOCIETY OF CHEMISTRY

PAPER

View Article Online
View Journal | View Issue

Check for updates

Cite this: *RSC Adv.*, 2023, **13**, 19651

# Enhancement in the electrical transport properties of $CaMnO_3$ *via* La/Dy co-doping for improved thermoelectric performance†

Ammu Vijay, *[a] Charan Prasanth S, [a] Roshan Jose[b] and Venkata Saravanan K[a]

The untiring endeavour towards green energy is a trending research among the research community. Thermoelectric materials are of vital importance here owing to their emission-free operation. As a righteous candidate, calcium manganate materials are being explored to increase its figure of merit. In this study, the structural, microstructural, electrical transport, and high-temperature thermoelectric measurements of $La_xDy_xCa_{1-2x}MnO_3$ {$x$ = 0.025 (L25D25), 0.05 (L50D50), 0.075 (L75D75), and 0.1 (L100D100)} were systematically performed. The structural confirmation of the synthesised sample was validated using X-ray diffraction, which also revealed the orthorhombic (space group: *Pnma*) crystallisation of co-doped samples with no traces of secondary peaks. A significant increase in the unit cell volume was observed with rare earth substitutions. The morphological studies revealed that the prepared samples were highly dense and the grain size was reduced with rare earth concentration. The substitution of La and Dy enhanced the conductivity values of pristine CMO by two orders of magnitude due to the high concentration of charge carriers and the presence of $Mn^{3+}$ ions due to rare earth doping. The conductivity increased with rare earth concentrations but diminished for $x = 0.1$ due to the localization of charges. The Seebeck coefficient values were negative for all the prepared samples, indicating electrons as the predominant carriers over the entire operating range. A minimum $\kappa$ of 1.8 W $m^{-1}$ $K^{-1}$ was achieved for $La_{0.1}Dy_{0.1}Ca_{0.8}MnO_3$ and the maximum value $zT$ obtained was 0.122 at 1070 K for $La_{0.075}Dy_{0.075}Ca_{0.85}MnO_3$.

Received 8th May 2023
Accepted 8th June 2023

DOI: 10.1039/d3ra03053a

rsc.li/rsc-advances

## Introduction

The demand for a sustainable energy source has been an inevitable concern of humanity for decades. The escalating environmental issues, cost, and demand for fossil fuels insist the need for a supplementary green energy source. According to the International Energy Outlook (IEO) 2016,[1] a hike of 48% in energy utilisation is expected from 2012 to 2040, resulting in hundreds of millions of people being devoid of essential energy services around 2040. The usage of conventional energy sources has to be reduced by the invention of new technologies to lessen the direct and indirect threats to nature, such as greenhouse gas emissions, climatic changes, and ozone depletion caused by fossil fuel consumption.[2] A large amount of waste heat is discarded into the environment due to chemical reactions, combustion of fossil fuels, industry wastages, *etc.*, which can be reused as useful energy. In automobiles, only 25% of the fuel is used for mobility and accessories and the rest of the fuel is going in vain as waste heat. The waste heat energy can be exploited using the thermoelectric effect, pyroelectric effect, or storage with phase transition materials.[3,4]

Thermoelectric materials provide cleaner energy by tackling waste heat in any form and converting it to electricity. The significant advantages of thermoelectric (TE) devices over other types of power generation devices are their emission-less operation, compactness, and absence of moving parts. Owing to these advantages, TE devices have extensive applications in automobiles, military, space, power generation, refrigeration *etc.*[5] and thus have become one of the research hotspots nowadays. A typical thermoelectric device consists of n-type and p-type thermoelectric materials connected electrically in series and thermally in parallel. The efficacy of a thermoelectric material can be deduced from the value of their dimensionless thermoelectric figure of merit, $zT$.

$$zT = \frac{S^2\sigma}{\kappa}T \tag{1}$$

in which $S$ refers to the Seebeck coefficient (μV $K^{-1}$), $\sigma$ refers to the electrical conductivity (S $cm^{-1}$), $\kappa$ refers to the thermal conductivity (μW $m^{-1}$ $K^{-1}$), and $T$ refers to the operating temperature (K).[6] For degenerate semiconductors, the

---

[a] Department of Physics, School of Basic and Applied Sciences, Central University of Tamil Nadu, Thiruvarur, 610 005, India. E-mail: ammuvijay.vijay@gmail.com

[b] Department of Science and Humanities, MLR Institute of Technology, Hyderabad, 500 043, India

† Electronic supplementary information (ESI) available. See DOI: https://doi.org/10.1039/d3ra03053a

expression for the Seebeck coefficient can be defined by the following expression.

$$S = \left(\frac{8\pi^2 k_B{}^2 m^* T}{3eh^2}\right)\left(\frac{\pi}{3n}\right)^{2/3} \tag{2}$$

where $k_B$ is the Boltzmann constant ($1.38 \times 10^{-23}$ J K$^{-1}$), $e$ is the electric charge ($1.6 \times 10^{-19}$ C), $h$ is the Planck's constant ($6.63 \times 10^{-34}$ J s$^{-1}$), $m^*$ is the effective mass of the carrier, $T$ is the temperature and $n$ is the carrier concentration. Thus, the Seebeck coefficient can be increased by increasing the effective mass and/or by decreasing the carrier concentration. The electrical conductivity can be improved by increasing the carrier concentration and/or carrier mobility, as given by eqn (3);

$$\sigma = ne\mu \tag{3}$$

The thermal conductivity comprises lattice thermal conductivity ($\kappa_l$) and electronic thermal conductivity ($\kappa_e$).

$$\kappa = \kappa_e + \kappa_l \tag{4}$$

Improvement in thermoelectric properties can be achieved either by increasing the power factor ($S^2\sigma$) or by reducing the thermal conductivity, especially the lattice contribution to thermal conductivity ($\kappa_l$). The lattice thermal conductivity depends mainly on crystal lattice disorder scattering, Umklapp scattering, and mass-difference impurity scattering.[7] An ideal thermoelectric material should have a considerable value of power factor ($S^2\sigma$) and low thermal conductivity, but their dependence on carrier concentration hinders the growth of the figure of merit.

The main limitations among high $zT$ state-of-the-art intermetallic compounds and alloys such as SiGe, $Bi_2Te_3$, PbTe, chalcogenides, and skutterudites include melting of constituent elements, decomposition, vaporisation or oxidation at elevated temperatures. Meanwhile, oxide thermoelectric materials are exploited due to their thermal and chemical stability at higher temperature regions. Despite the advantages mentioned above, oxide thermoelectric materials give poor thermoelectric performance because of the localisation of electrons accompanied by low carrier mobility, which is caused by the strong ionic character with narrow conduction bandwidths arising from weak orbital overlap.[8] The incompatible characteristics of oxide materials in the group of thermoelectric materials were overcome by the study of $Na_xCoO_2$ in 1997, which has a moderate value of Seebeck coefficient (100 μV K$^{-1}$) and low value of electrical resistivity (0.2 mΩ cm) at room temperature.[9] An ample choice for oxide thermoelectric materials is available, and several kinds of research are ongoing to increase their thermoelectric performance. As the development of n-type materials is far behind that of p-type counterparts, much more prolific research is necessary for the improvement of the thermoelectric properties of n-type materials.

Our work deals with the $\sigma$ modification and thermoelectrical properties of an n-type perovskite $CaMnO_3$, a G-type antiferromagnetic insulator with Néel temperature $T_N = 110$ K. It has a perovskite orthorhombic structure ($\sqrt{2}a_c$, $2a_c$, $\sqrt{2}a_c$). Reduction in oxygen content results in a weak ferromagnetic behaviour of $CaMnO_{3-\delta}$, accompanied by an enhancement in Néel's temperature and conductivity. These are due to the incorporation of $Mn^{3+}$ ions, which paves a double exchange mechanism between $Mn^{3+}$–O–$Mn^{4+}$ and conduction by electron hopping. The $e_g$ states in the $Mn^{4+}$ ($d^3 \rightarrow t_{2g}^3 e_g^0$) ion are vacant, and electrons will occupy $e_g$ states when they are introduced in the system and thereby generate $Mn^{3+}$ ions.[10,11] The electrical properties in $CaMnO_3$ are due to Mn 3d states and Op states. The central part of carrier transport occurs in the Mn–O1 (equatorial oxygen) since it possesses a higher hybridisation degree than Mn–O2 (axial oxygen). Thus, any vacancies associated with O1 affect the conduction path to reduce carrier mobility. The oxygen vacancies will change Mn valence states from 4p to 3p, which makes Mn $e_g$ orbital partially filled and thereby cause Jahn–Teller distortion.[12] Being an n-type semiconductor, CMO is known for its moderate value of the Seebeck coefficient and low electrical conductivity. However, its $zT$ value is relatively low due to high thermal conductivity (~5 W m$^{-1}$ K$^{-1}$).[13] Different strategies were employed in the literature to achieve a higher figure of merit, such as trivalent substitution at the $Ca^{2+}$ site,—to enhance the electrical transport properties—and co-doping at the Ca site, —to enhance the thermoelectric properties,—which is comparatively less in number. Co-doping at the Ca site can simultaneously decrease both resistivity and thermal conductivity and hence is considered to be more effective than single doping.[14,15] J. W. Seo *et al.*[16] studied the electric and thermoelectric properties of Y, Dy co-doped CMO. Furthermore, the thermoelectric properties of La, Er,[17] La, Ce,[18] La, Sr[19] La, and Sm[20] co-doped CMO were investigated in detail for gaining superior thermoelectric properties.

The present work comprehends the structural, transport, and thermoelectric properties of lanthanum (La) and dysprosium (Dy) co-doped calcium manganate, $CaMnO_3$. This strategy was employed to reduce the thermal conductivity of the samples by introducing more scattering centres into the system in line with the distortion caused by La and Dy. The two dopants La and Dy were simultaneously doped ($La_xDy_xCa_{1-2x}MnO_3$) with carrier concentrations of 0.05 to 0.2 to observe their effect of them on the thermoelectric properties of CMO. The rare earth substitutions in the Ca site induce $Mn^{3+}$ in the $Mn^{4+}$ matrix with electron doping in $e_g$ states. In addition, the significant mass difference between Ca, La, and Dy is beneficial for the excitation of local phonon modes around doping centres and strong phonon scattering, favouring the reduction in thermal diffusivity. Thus a good enhancement in the thermoelectric figure of merit is anticipated through the solid-state synthesised $La_xDy_xCa_{1-2x}MnO_3$.

## Experimental

### Sample preparation

A conventional solid-state reaction was implemented for the synthesis of polycrystalline bulk samples of lanthanum (La) and dysprosium (Dy) co-doped CMO; $La_xDy_yCa_{1-x-y}MnO_3$ ($x = 0.025$, 0.05, 0.075 and 0.1). For each composition of $La_xDy_yCa_{1-x-y}MnO_3$, stoichiometric quantities of $CaCO_3$ (≥99%, Sigma-

Aldrich), $MnO_2$ (>99%, Sigma-Aldrich), $La_2O_3$ (99.9, Himedia), and $Dy_2O_3$ (Sigma-Aldrich) were thoroughly mixed using a planetary ball mill (Fritsch, Pulverisette 5/4 classic line) for 12 hours. To aid homogenisation, ethanol was added to the mixture while grinding. The obtained slurry was dried in the hot air oven overnight at 80 °C for the evaporation of ethanol. The samples were taken out and crushed using mortar and pestle. The powder was heated at 1173 K for 12 hours for the calcination of the mixture by decarbonisation of $CaCO_3$. The calcined powder was attrition milled at the same duration at a higher rpm to form a narrow grain size distribution. The powder was sieved and compacted into cylindrical pellets of different dimensions using a uniaxial press with a pressure of 4–5 tons, and sintered at 1573 K for 12 hours in the air and cooled in the furnace to room temperature.

### Material characterisation

X-ray diffraction was carried out using Malvern Panalytical X'Pert3 equipped with a Cu Kα ($\lambda = 0.15406$ nm) source at room temperature and data were collected over the range of $20° \leq 2\theta \leq 90°$ for the structure and phase analysis. The structural parameters were obtained by the Rietveld Refinement of X-ray Diffraction (XRD) using the FULLPROF package.[21] The densities of the sintered samples were measured using the Archimedes method. Relative densities were calculated from experimental density and theoretical density, which were derived from cell volume and molecular formula. The morphology of the synthesised samples was examined using Nova Nano FE-SEM 450 (FEI). The oxidation states of manganese in the sintered bulk ground to powder were determined using an X-ray photoelectron spectrometer (XPS) (PHI VersaProbe III) equipped with a monochromatic Al Kα source. C 1s at 285.0 eV was used as the binding energy reference. The high-temperature simultaneous measurement of Seebeck coefficient ($S$) and electrical conductivity ($\sigma$) was performed in a nitrogen atmosphere using the NETZSCH SBA 458 Nemesis equipment (the errors for Seebeck coefficient and electrical conductivity are ±7% and ±5%, respectively. The repeatability for both Seebeck coefficient and electrical conductivity are ±3%). Specific heat measurements were taken in a nitrogen atmosphere using NETZSCH DSC404 Pegasus. Disc-shaped pellets were coated thoroughly with graphite for the measurement of thermal diffusivity from 373 K to 1173 K using NETZSCH LFA 457 Microflas in a nitrogen atmosphere.

## Results and discussion

### X-ray diffraction

The phase formation of the prepared compositions was confirmed using XRD analysis, and the XRD profiles for the same are presented in Fig. 1(i). The obtained diffraction peaks well matched with the standard data of $CaMnO_3$ in JCPDS card no. 76-1132. The absence of detectable impurity peaks in the recorded XRD patterns confirmed the phase purity of the co-doped samples. The diffraction peaks of all the samples correspond to the orthorhombic structure with symmetry of the *Pnma* space group (space group number: 62). The intensity of (101) crystal plane was found to decrease with rare earth substitution, depicting the lattice distortion[22] in the $La_xDy_xCa_{1-2x}MnO_3$ samples. $Mn^{3+}$ ions induced from the trivalent ion doping are the cause of Jahn–Teller (JT) distortion in the $MnO_6$ octahedra.

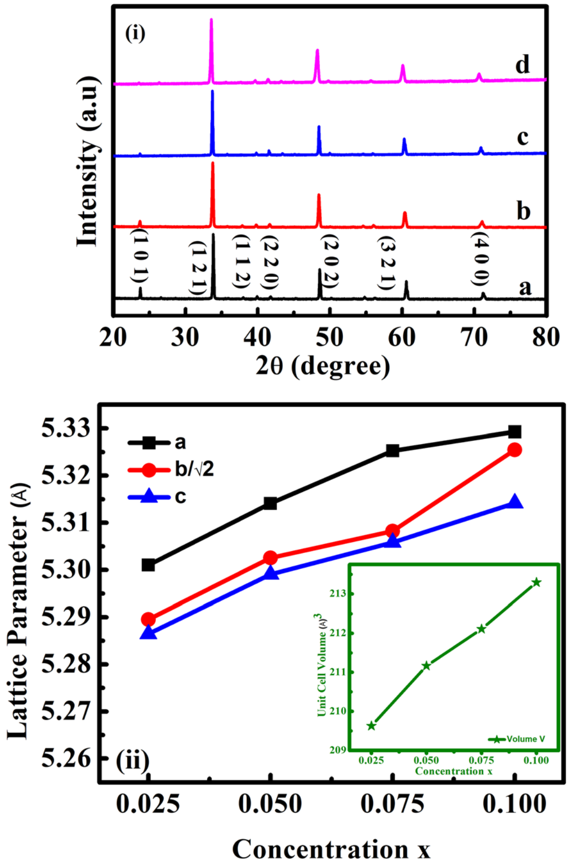

Fig. 1 (i) X-ray diffractograms and (ii) evolution of unit cell parameters and unit cell volume (inset) of $La_xDy_xCa_{1-2x}MnO_3$ co-doped samples, where $x$ = (a) 0.025, (b) 0.05, (c) 0.075 and (d) 0.1.

Distortion in $MnO_6$ octahedra can be evaluated from the peak shifting in the XRD pattern. A slight shift in the diffraction peaks towards the lower angle emphasizes that the unit cell volume has increased with rare earth substitution. The presence of $Ca^{2+}$, $La^{3+}$, and $Dy^{3+}$ ions, along with the larger $Mn^{3+}$ ions formed in the $Mn^{4+}$ matrix due to charge compensation enhanced the lattice volumes. Cell volume growth showed that the rare earth constituents entered the perovskite matrix. The lattice parameters were determined using FULLPROF.[21] The lattice parameter of CMO can be related to the lattice parameter, $a_{\text{ideal}}$ of ideal cubic perovskite structure by the relations: $a \approx \sqrt{2}a_{\text{ideal}}$, $b \approx 2a_{\text{ideal}}$, $c \approx \sqrt{2}a_{\text{ideal}}$. Thus $\sqrt{2}a \approx b \approx \sqrt{2}c$.[23] To show the structural deviation from the ideal cubic, $a$, $b/\sqrt{2}$, and $c$ were plotted and are given in Fig. 1(ii). The increase in the values of '$a$' with RE substitution is greater than that of '$b$' and '$c$', which governed the reduction in orthorhombic distortion. Furthermore, the lattice parameters obey the relation $c < b/\sqrt{2} < a$, which corresponded to the O-type orthorhombic structure. The

Table 1 Variation in lattice parameters, reliability parameters, and unit cell volumes of $La_xDy_xCa_{1-2x}MnO_3$ co-doped samples

| Parameters/composition | L25D25 | L50D50 | L75D75 | L100D100 |
|---|---|---|---|---|
| $a$ (Å) | 5.301 | 5.314 | 5.325 | 5.329 |
| $b$ (Å) | 7.480 | 7.499 | 7.507 | 7.531 |
| $c$ (Å) | 5.286 | 5.299 | 5.306 | 5.314 |
| $\chi^2$ | 5.10 | 2.66 | 2.39 | 8.23 |
| Bragg $R$ factor | 2.19 | 1.88 | 2.33 | 3.09 |
| $R_f$ factor | 2.05 | 2.17 | 2.82 | 3.26 |
| Volume (Å$^3$) | 209.6 | 211.2 | 212.1 | 213.3 |
| Theoretical density (g cm$^{-3}$) | 4.706 | 4.846 | 4.998 | 5.143 |
| Experimental density (g cm$^{-3}$) | 4.6 | 4.721 | 4.933 | 5.14 |
| Relative density (%) | 97.7 | 97.4 | 98.7 | 99.9 |

reliability factors and the variation in lattice parameters are tabulated and presented in Table 1.

## Scanning electron microscopy

SEM micrographs of the sintered pellets are given in Fig. 2. Morphological examination revealed well-densified pellets with polygon-shaped grains. All the surface structures are found to be compact without the presence of any apparent cracks and crevices, which is pointed to a homogeneous microstructure with high relative density. The grain size distribution of each composition was determined using ImageJ software, and the plot is shown in the insets of corresponding compositions. The average grain sizes were 6.4 μm, 3.4 μm, 2.8 μm, and 2.6 μm for L25D25, L50D50, L75D75, and L100D100, respectively.

As the concentration of rare earth elements increased, the grain size decreased, indicating that lanthanum and dysprosium inhibited grain growth in the sintered samples. The small grain size or a large number of grain boundaries with higher rare earth doping can increase the scattering centre and thereby reduce the thermal conductivity. In order to support the results, the density, $d$ of the sintered samples was measured using Archimedes principle. The theoretical density $d_t$ of each CMO-based composition was determined using the formula given below:

$$d_t = \frac{4M}{N_A V} \tag{5}$$

where $M$, $N_A$, and $V$ are the molecular weight (g mol$^{-1}$), Avogadro's number ($6.022 \times 10^{23}$), and unit cell volume (cm$^{-3}$).

Thus, relative density, $d_{rel}$ was calculated using the relation $d_{rel} = d/d_t \times 100$. The density and the relative density values were enhanced with the rare earth contents, which corroborates the SEM results. The theoretical density values are included in Table 1.

## XPS

To further emphasize the inference from the XRD that the La/Dy co-doping induced $Mn^{3+}$ ions in the matrix, XPS analysis was carried out. Fig. 3 depicts the XPS spectra of Mn $2p_{3/2}$ peaks of

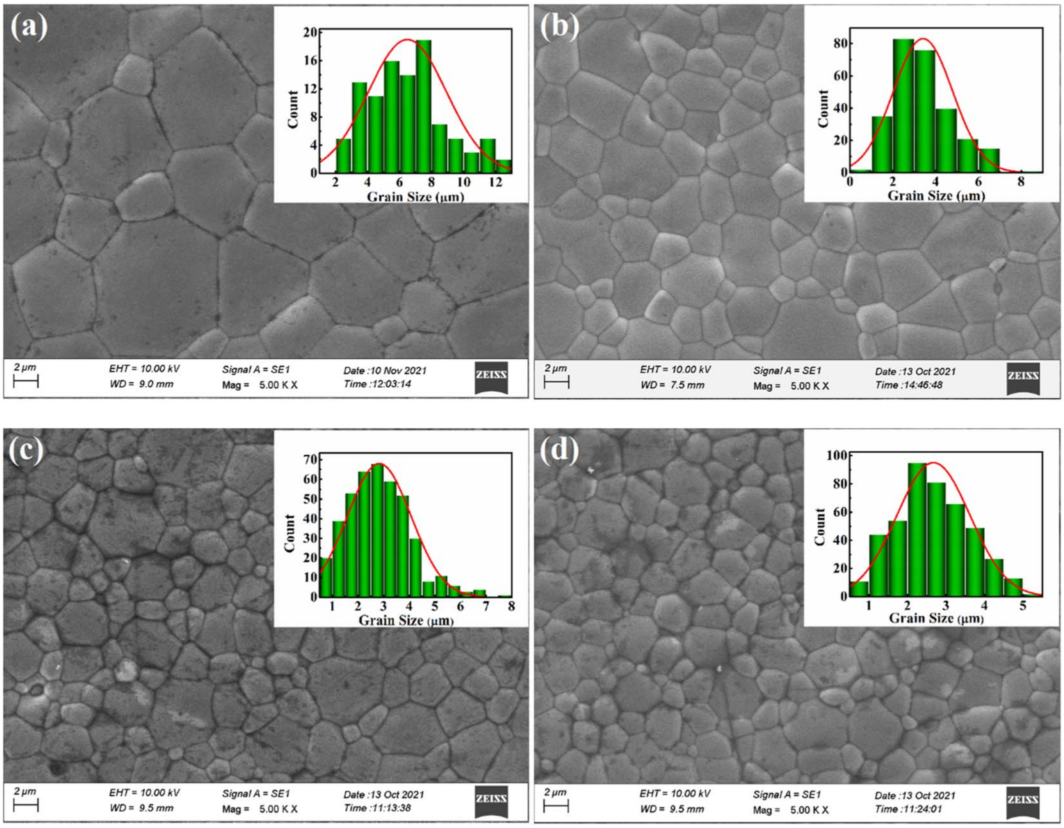

Fig. 2 SEM micrographs attained from the surfaces of $La_xDy_xCa_{1-2x}MnO_3$ sintered pellets with $x$ = (a) 0.025, (b) 0.05, (c) 0.075 and (d) 0.1.

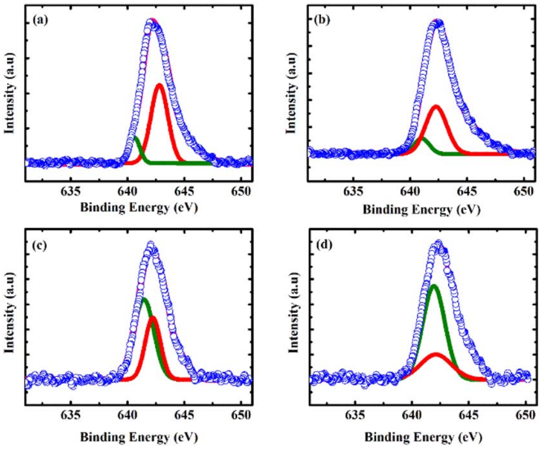

Fig. 3 XPS spectra of Mn $2p_{3/2}$ in the $x$ = (a) 0.025, (b) 0.05, (c) 0.075 and (d) 0.1 $La_xDy_xCa_{1-2x}MnO_3$ samples. Olive colour and red colour corresponds to the peaks of $Mn^{3+}$ and $Mn^{4+}$, respectively.

La/Dy co-doped CMO samples. The spectrum revealed the existence of both $Mn^{3+}$ (represented by the peak at the low binding energy side of the Mn $2p_{3/2}$ peak) and $Mn^{4+}$ in the prepared samples. It can be seen that the valence states of Mn are affected by co-doping by analyzing the area under deconvoluted peaks. Thus co-doping at the Ca site induces larger $Mn^{3+}$ ions in the $Mn^{4+}$ matrix, which is beneficial for the hopping conduction in CMO.[24] Hence, this result corroborates the enhancement in the lattice volume and the effects of conductivity measurements (which will be discussed in the next section). The contributions of $Mn^{3+}$ and $Mn^{4+}$ observed from the binding energy values of Mn $2p_{3/2}$ are given in Table 2.

The binding energy values of Mn oxidation states in the Mn $2p_{3/2}$ electronic state observed results of XPS are in good agreement with the reported studies showing the existence of two oxidation states of Mn. Thus, the transport properties of the doped manganites can be altered by the varying oxidation state of Mn.[19,25–29]

### Electrical transport properties

Fig. 4(i) illustrates the evolution of electrical conductivity with temperature. The samples prepared in this study showed higher conductivity values than those of pristine CMO.[20] A two-order increment $\sigma$ was obtained for L75D75 and L100D100. $La^{3+}$ and $Dy^{3+}$ ions contribute significant changes in the electrical conductivity of CMO by facilitating the hopping between $Mn^{3+}$ and $Mn^{4+}$ ions. Electrical conductivity values were enhanced by adding rare earth elements to the Ca-site. Furthermore, $\sigma$ for L75D75 and L100D100 decreased with temperature, depicting a metallic behavior. These samples' metallic conduction ($d\sigma/dT < 0$) is due to the high $Mn^{3+}/Mn^{4+}$ ratios. Also, more electrons fill $e_g$ orbitals with co-doping, which can widen the $e_g$ orbital to an itinerant band, and the conduction mechanism will be metallic-like.[30] The charge-ordering phenomenon may be the possible reason for the reduction in the electrical conductivity of L100D100.[31,32] Metal-to-insulator transition (MIT) was observed in every sample prepared, especially at high concentrations of rare earth elements.[33] Electrical conductivity was found to decrease after a certain temperature for a high value of co-doping resulting in metallic behaviour. The delocalisation character of $e_g$ electrons derived from the partial $t_{2g}$ electrons of the $Mn^{3+}$ ion above the metal-insulator transition is the possible reason for the metallic behaviour. The change in the crystal field splitting

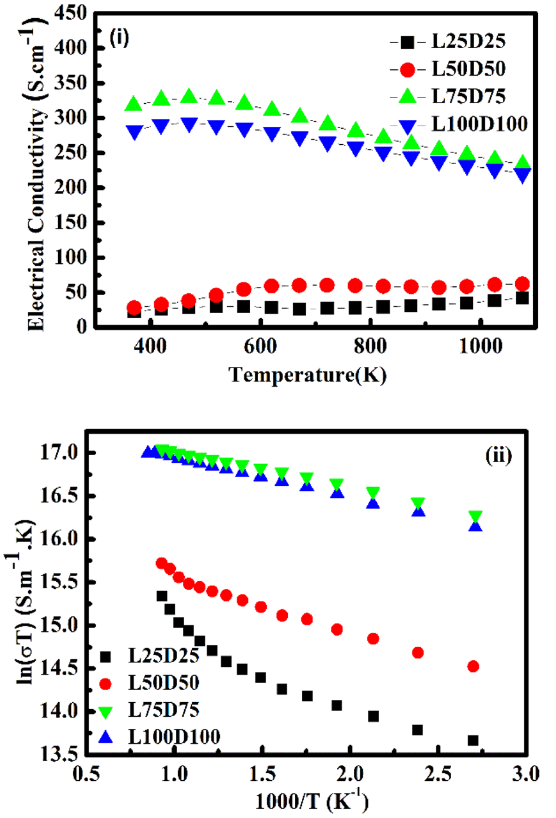

Fig. 4 (i) Temperature dependence of the electrical conductivity, (ii) plot of ln($\sigma T$) *vs.* 1000/$T$.

Table 2 Spectral fitting parameters of Mn $2p_{3/2}$ (peak positions and peak area of $Mn^{3+}$ and $Mn^{4+}$)

| Sample code | Mn $2p_{3/2}$ binding energy of $Mn^{3+}$ (eV) | Mn $2p_{3/2}$ binding energy of $Mn^{4+}$ (eV) | Mn $2p_{3/2}$ peak area of $Mn^{3+}$ | Mn $2p_{3/2}$ peak area of $Mn^{4+}$ |
|---|---|---|---|---|
| L25D25 | 640.62 | 642.81 | 439.38 | 2104.84 |
| L50D50 | 641.02 | 642.28 | 476.73 | 2052.89 |
| L75D75 | 641.44 | 642.23 | 1414.69 | 832.09 |
| L100D100 | 641.93 | 642.11 | 1834.57 | 685.65 |

energy ($\varDelta_0$) and exchange splitting energy ($E_{ex}$) will be affected by the distortion of $MnO_6$ octahedra. The value of $E_{ex}$ is higher than that of $\varDelta_0$ in the ground state of perovskite manganates than the electronic configuration of $Mn^{3+}$ is in the HS state. As the temperature increases the electrons in the $e_g$ orbital gain energy and go to the $t_{2g}$ orbital so as to form $t_{2g}^4 e_g^0$, which is the LS state.[15,34] The observed change in the $T_{MI}$ indicates a change in the $Mn^{3+}$ content in the co-doped manganates,[35] which can be ascribed to the charge ordering in these species. The metal-to-insulator transition temperature was slightly increased with increasing the doping concentrations. This may be attributed to the increase in the grain boundaries and there by insulating nature at high concentration of dopants in the system, which is evident from the SEM images.

**Conduction mechanism.** The general mechanism for conduction in the manganate family is the adiabatic small polaron hopping mechanism between $Mn^{4+}$ and $Mn^{3+}$, which is formed as a result of charge compensation and $O^{2-}$. The hopping of charge carriers is thermally activated with the activation energy $E_a$,[36] and the expression for electric conductivity is given by

$$\sigma = \sigma_0 \exp\left(\frac{-E_a}{k_B T}\right) \tag{6}$$

where $\sigma_0$ and $A$ are constants and $k_B$ is the Boltzmann constant.

In the high-temperature region, $Mn^{4+}$ will be reduced to $Mn^{3+}$ by creating oxygen vacancies and thereby charge carriers. Kröger–Vink notation for the charge neutrality is as follows[37]

$$O_O^{\times} = V_O^{\cdot\cdot} + \frac{1}{2}O_2 + 2e^- \tag{7}$$

$$Mn^{4+}_{lattice} + 4O^{2-}_{lattice} = V_O^{\cdot\cdot} + \frac{1}{2}O_2 + 2Mn^{3+}_{lattice} + 3O^{2-}_{lattice} \tag{8}$$

It could be seen that the conductivity values follow the adiabatic small polaron transport model for all the samples. Fig. 4(ii) illustrates the dependency of $\log(\sigma T)$ with $1/T$. The trend of the graph is found to be linear, indicating the conduction is obeying the adiabatic small polaron transport model. The linearity observed can be attributed to the hopping motion of charge carriers and polarons across localised states or within the bands.[38] Deducing the slope of linear fitted data gave activation energy for every co-doped sample. The activation energy is found to be decreasing with the increase in the concentration of rare earth elements.

In addition, the electrical conductivity in manganites can also change by the variation of the effective one-electron bandwidth ($W$), or $e_g$ electron transfer interaction that is altered by the change in tolerance factor.[39] The magnitude of distortion in the samples can be quantified using the equation given below:

$$t = \frac{r_A + r_O}{\sqrt{2(r_B + r_O)}} \tag{9}$$

where $r_A$, $r_B$, and $r_O$ represent the ionic radii of A-site, B-site, and oxide ions, respectively. The ionic radii of $Ca^{2+}$, $La^{3+}$, $Dy^{3+}$, $Mn^{3+}$, and $Mn^{4+}$ used for calculating tolerance factor are (C.N XII) 1.34 Å, (C.N XII) 1.36 Å, (C.N VI) 0.912 Å, (C.N VI) 0.645 Å and (C.N VI) 0.53 Å, respectively.[40] The increased distortion occurs due to the change of Ca to La/Dy/Ca and $Mn^{4+}$ to $Mn^{3+}$. A decrease of 2% was observed in the values of '$t$'. Furthermore, as the concentration of rare earth constituents decreases, '$t$' tends to unity, which implies distortion of $MnO_6$ octahedra is comparatively lower than the co-doped versions of CMO with higher concentrations of La and Dy. The calculated values of the tolerance factor along with deduced activation energy from electrical conductivity measurements are tabulated in Table 3.

It is worth noting that all the $Mn^{4+}$ present in the co-doped CMO system does not participate in the hopping mechanism. Hopping facilitates charge carrier transport only when the spin directions of $Mn^{3+}$ and $Mn^{4+}$ are in the same direction. The polaron hopping does not occur if the spin direction of $Mn^{4+}$ is opposite to that of $Mn^{3+}$.[41] Fig. 5 (top) illustrates the electron transport between $Mn^{3+}$ and $Mn^{4+}$ with opposite spins through $O^{2-}$. According to Hund's rule, such a transition does not occur in CMO systems since the resultant state ($S_z$) would be highly excited.

Meanwhile, the electron transport with spins of the same direction in $Mn^{3+}$ and $Mn^{4+}$ requires comparatively lower energy than the previous one. The spin direction before and after hopping does not change in this case. This is in good agreement with the low values of $E_a$.

### Seebeck coefficient

The evolution of the Seebeck coefficient with temperature for different La and Dy concentrations is shown in Fig. 6. A decreasing trend in the $S$ values with an increase in the rare earth elements concentration is observed as expected due to the increase in the carrier concentration. Moreover, a linear relationship of $S$ with $1/T$ (Fig. 7) was sustained in the entire temperature region for L75D75 and L100D100 but deviated at

Table 3 Values of $E_a$ and $E_s$ activation energy, polaron binding energy and tolerance factor of $La_xDy_xCa_{1-2x}MnO_3$ co-doped samples ($x = 0.025$, 0.05, 0.075 and 0.1)

| The concentration of rare earth elements | $E_a$ (meV) | $E_s$ (meV) | $W_p$ | $E_p$ | Tolerance factor $t$ |
|---|---|---|---|---|---|
| 0.025 | 69.93 | 49 | 20.93 | 10.46 | 0.997 |
| 0.05 | 51.42 | 40.96 | 10.46 | 5.23 | 0.990 |
| 0.075 | 40.05 | 33.81 | 6.24 | 3.12 | 0.984 |
| 0.1 | 40.2 | 32.38 | 7.82 | 3.91 | 0.977 |

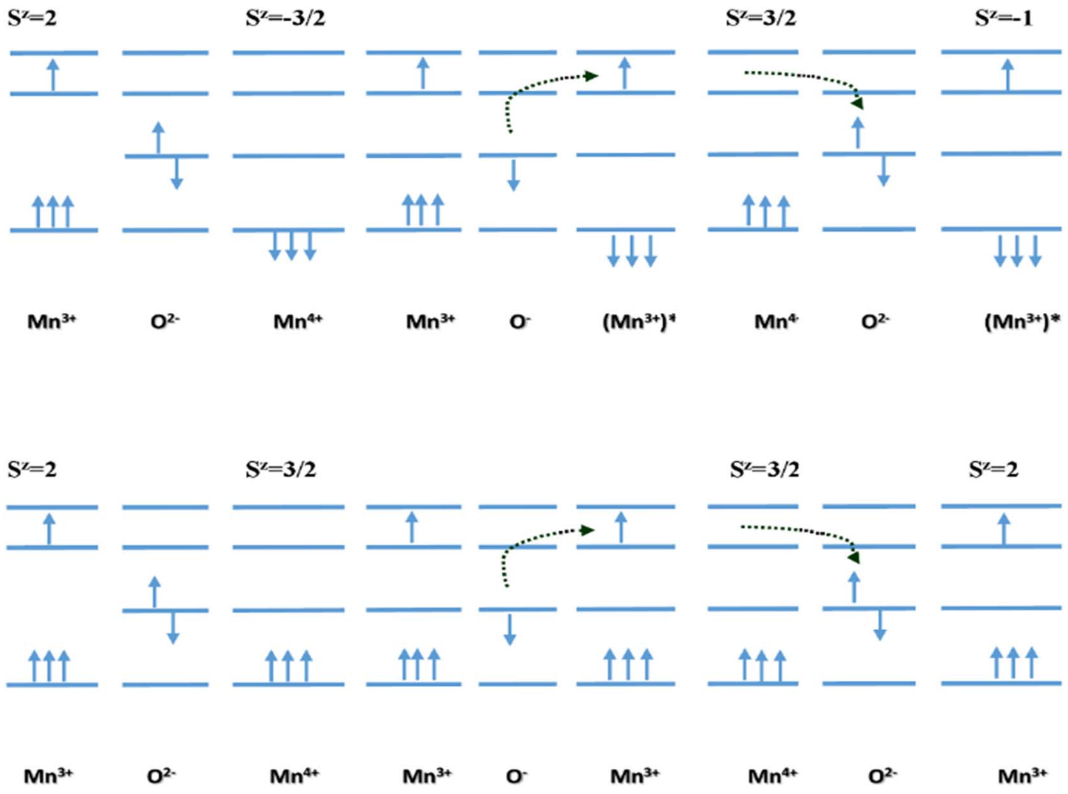

Fig. 5 Diagram illustrating electron transport between $Mn^{3+}$ and $Mn^{4+}$ having (top) opposite, and (bottom) equal spins.[41]

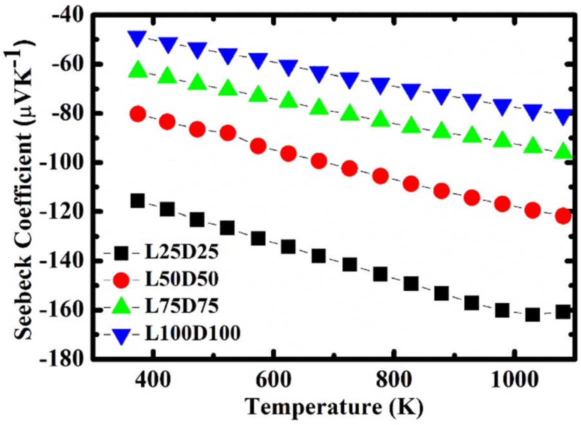

Fig. 6 Evolution of Seebeck coefficient with temperature.

high temperatures for the other two samples. The linearity observed in the plot affirms the hopping conduction satisfying Mott's adiabatic small polaron conduction model,[42] which is given by

$$S = \pm \frac{k_B}{e}\left(\frac{E_S}{kT} + A\right) \tag{10}$$

where $k_B$ is the Boltzmann constant, $e$ is the charge of the electron, $E_S$ is the thermopower activation energy, and $A$ is a dimensionless constant. The estimated activation energy $E_S$, was observed to be lower than $E_a$, which supports small polaron conduction behaviour in the manganite samples.

The reduction in the $E_S$ values with rare earth substitution can be attributed to the decrease in the width of the polaron band gap as the increase in $Mn^{3+}$ ions. $E_a$ is the sum of the activation energy needed to create the carriers and activate the hopping of carriers, and $E_S$ is the energy required for the activation of the hopping of carriers. Hence, $E_S$ is much smaller than $E_a$. The polaronic hopping energy $W_p$ and polaron binding energy $E_p$ can be calculated from the values of $E_a$ and $E_S$.[43]

The polaron hopping energy $W_p$ is described by

$$W_p = E_a - E_S \tag{11}$$

The polaron binding energy $E_p = 2W_p$.[44,45] The parameters determined from Seebeck measurements are given in Table 3.

The strong decline in absolute values of the Seebeck coefficient at high-temperature emphasizes that the samples become oxygen deficient, which results in the enhancement of charge carrier concentration.[46] The onset of transition from *ortho* ↔ *tetra* is evident in Fig. 6. An apparent change in the $|S|$ values of L25D25 observed at high temperatures emphasizes this phenomenon. The trend is absent in other samples due to the increase of structural transition temperature with doping concentration.

The high temperature ($k_B \gg E_s$) limit of the Seebeck coefficient can be resolved from $S(T)$ curves using Heikes and Marsh *et al.*'s[47] models and is stated as follows:

$$S = \left(-\frac{k_B}{e}\right)\ln\left(\frac{3-p-x}{p-1+x}\right) \tag{12}$$

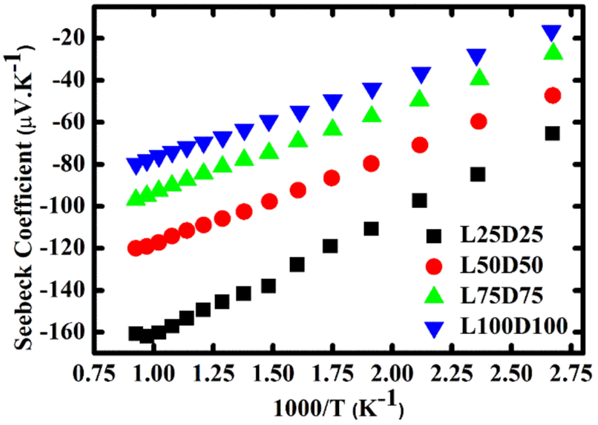

Fig. 7 Plot of $S$ *vs.* 1000/$T$.

where $p$ is the average number of e$_g$ electrons per Mn$^{3+}$ ion and $x$ is the electron concentration. As shown in Fig. 8, the average e$_g$ electrons in Mn$^{3+}$ ions are not one, but between 1.2 and 1.5 at high temperatures, that depicts the enhancement in the conductivity mechanism. Mn$^{3+}$ is having one electron in e$_g$ orbital. As the temperature increases, t$_{2g}$ electrons gain more energy and they can be activated to e$_g$ orbitals, which cause improvement in '$p$' values. For $x > 0.10$, '$p$' values are in the range 1.3–1.5. Y. Wang *et al.*[42] suggested a more likely reason for the growth of an average number of e$_g$ electrons with '$x$'. To release the energy of the elongated Mn$^{3+}$O$_6$ octahedron due to increased Mn$^{3+}$–O–Mn$^{4+}$ hopping, more t$_{2g}$ electrons will be activated to e$_g$ orbital since that activation energy is lower than the energy in octahedron distortions. Consequently, more number of electrons exist in e$_g$ orbital, which eventually increases '$p$'. The obtained values of '$p$' in the present study are slightly greater than that in the work of Y. Wang *et al.* (La-doped CMO) where the '$p$' values are in the range 1.1–1.4.

### Power factor

The power factor ($S^2\sigma$) of the prepared samples was calculated and plotted in Fig. 9. Power factors are enhanced with temperature. However, a drop in the power factor at a high temperature of L50D50 was observed, which is due to the reduction in the Seebeck coefficient of the same. L75d75 showed the maximum value of power factor among the samples prepared. The maximum values of power factor for L25D25, L50D50, L75D75 and, L100D100 are 125.56 μW m$^{-1}$ K$^{-2}$, 93 μW m$^{-1}$ K$^{-2}$, 217 μW m$^{-1}$ K$^{-2}$ and 140.32 μW m$^{-1}$ K$^{-2}$, respectively, at 1126 K. The observed values are significantly higher than the power factor values of CMO, which emphasise that the La/Dy co-doping strategy will further increase its $zT$ due to the improvement in the electrical transport properties.

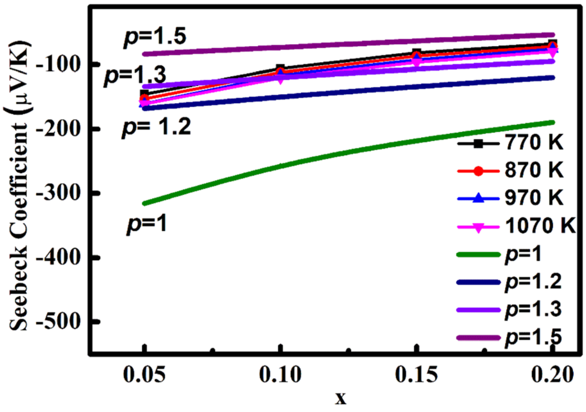

Fig. 8 Variation in $S$ with carrier concentration at different temperature. Calculated curves of different '$p$' values are also shown.

### Thermal conductivity

The temperature dependence of total thermal conductivity $\kappa$ and lattice thermal conductivity $\kappa_l$ (inset) of La/Dy co-doped CMO samples are shown in Fig. 10. The minimum thermal conductivity was achieved for the L100D100 sample, which is due to the presence of a higher number of grain boundaries and larger Mn$^{3+}$ ions, and rare earth ions in addition to the ions in CMO. The obtained thermal conductivity values are lower than those of the Dy-doped CMO.[48] The electronic thermal

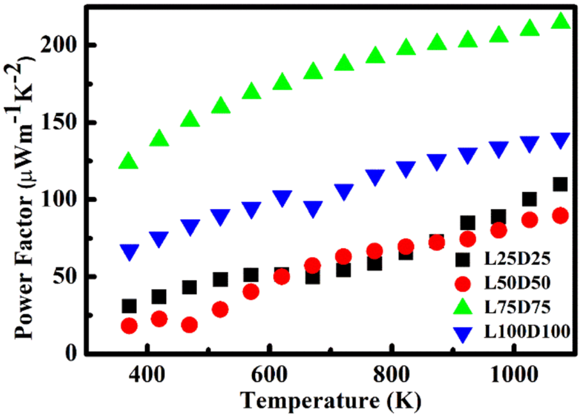

Fig. 9 Evolution of power factor with temperature.

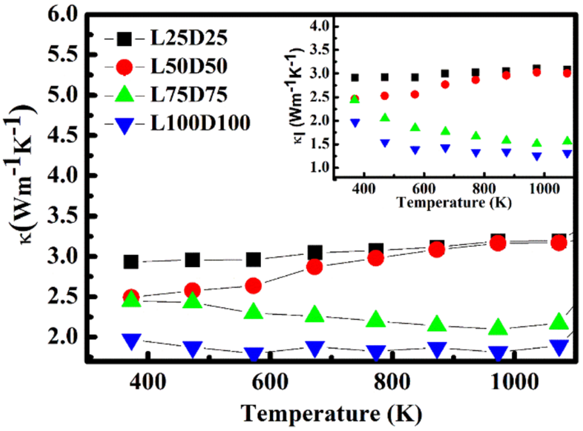

Fig. 10 Temperature dependence of total thermal conductivity, and lattice thermal conductivity (inset).

conductivity, $\kappa_e$ (Fig. 11) was calculated from the obtained thermal conductivity using Weidemann–Franz law,[49]

$$\frac{\kappa_e}{\sigma} = LT \tag{13}$$

where $L$ is the Lorentz number ($2.45 \times 10^{-8}$ V$^2$ K$^{-2}$). Furthermore, the total thermal conductivity $\kappa$ is the sum of the lattice thermal conductivity, $\kappa_l$, and electronic thermal conductivity $\kappa_e$ (eqn (4)).

It can be inferred from Fig. 10 that the difference between $\kappa$ and $\kappa_l$ is negligible. Hence $\kappa_l$ contributes larger to the total thermal conductivity, whereas $\kappa_e$ involvement is significantly less. $\kappa_e$ values increase with temperature and doping concentration due to its dependence on electrical conductivity.

SEM images clarify that the sample consists of no noticeable pores, which implies that the samples are well-densified. Thus, the reduction in thermal conductivity of co-doped samples to that of the pure CMO (~5 W m$^{-1}$ K$^{-2}$)[13] is due to the phonon scattering.

The larger mass of rare earth ions and bigger-sized Mn$^{3+}$ ions are the notable reasons for the reduction in thermal conductivity in addition to the increase in grain boundaries with co-doping. The significant change in the ionic radius and mass makes the ions scattering centres reduce the phonon mean free path.

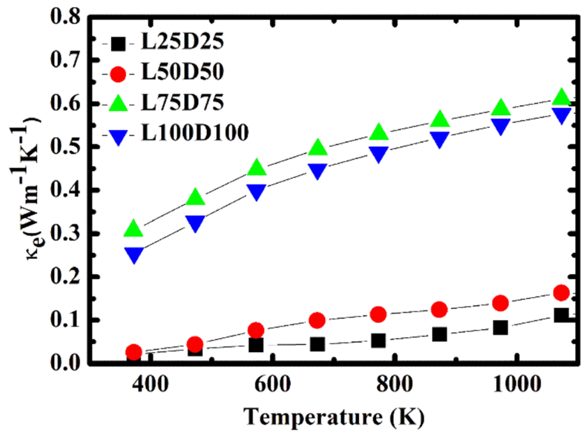

Fig. 11 Temperature dependence of electronic thermal conductivity.

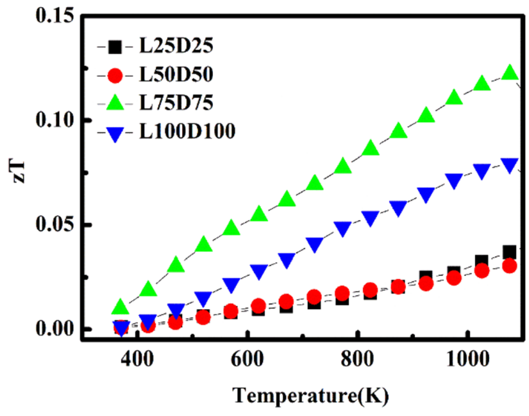

Fig. 12 Evolution of dimensionless figure of merit, $zT$ of La$_x$Dy$_x$Ca$_{1-2x}$MnO$_3$ ceramics.

Table 4 Comparison of power factor and $zT$ of present work with previously reported studies on CMO

| Composition | Power factor (μW m$^{-1}$ K$^{-2}$) | $zT$ | Reference |
|---|---|---|---|
| $Yb_{0.1}Dy_{0.02}Ca_{0.88}MnO_3$ | 300 | 0.11 | 50 |
| $Na_{0.05}Dy_{0.05}Ca_{0.9}MnO_3$ | 280 | 0.11 | 51 |
| $Ca_{0.98}Dy_{0.02}MnNb_{0.02}O_3$ | 258 | 0.08 | 52 |
| $La_{0.075}Dy_{0.075}Ca_{0.85}MnO_3$ | 217 | 0.12 | This work |

### *zT*

The evolution of the figure of merit, $zT$ of La/Dy co-doped CMO samples with temperature is shown in Fig. 12. Generally, $zT$ values increase with temperature and decline in the high-temperature regions due to the enhancement in thermal conductivity. The highest $zT$ value obtained was 0.122 at 1075 K for L75D75, which is due to the sample's high power factor and low thermal conductivity.

La/Dy co-doping improved the electrical performance of the samples, whereas the thermopower values got diminished due to the increased carrier concentration. The increase in '$p$' values corroborates these results. Co-doping of CMO with Dy and other elements of different ionic radii were also studied in detail by various researchers and the comparison of their $zT$ and PF with the present work is tabulated in Table 4.

## Conclusions

Single-phased La$_x$Dy$_x$Ca$_{1-2x}$MnO$_3$ ($x$ = 0.025, 0.05, 0.075, and 0.1) pellets were successfully prepared using the conventional solid-state reaction method. The structural and high-temperature transport and thermoelectrical properties were investigated thoroughly. The electrical conductivity increased significantly on La/Dy co-doping and lowered for $x$ = 0.1. The influence of co-doping reduced the thermal conductivity marginally and thereby making a remarkable change in $zT$ values compared to the reported values of the pure CMO. A maximum value of 0.122 at 1075 K was achieved for L75D75 ceramics.

## Author contributions

Ammu Vijay: methodology, software, writing – original draft, visualization, conceptualization, validation; Charan Prasanth S: writing – review and editing; Roshan Jose: writing – review and editing; Venkata Saravanan K: conceptualisation, resources, validation, supervision, writing – review, and editing.

## Conflicts of interest

There are no conflicts to declare.

## Acknowledgements

The work was supported by Science and Engineering Research Board, India (grant/award no. ECR/2015/000273). The authors acknowledge ACIC, St. Joseph's College, Tiruchirappalli, for SEM characterisation and NRC, SRM Institute of Science and Technology, Chennai for XPS analysis.

## References

1 P. Holtberg, J. Diefenderfer and A. LaRose, *International Energy Outlook 2016*, 2016.
2 L. E. Bell, *Science*, 2008, **321**, 1457–1461.
3 J. Yang and F. R. Stabler, *J. Electron. Mater.*, 2009, **38**, 1245–1251.
4 L. B. Kong, T. Li, H. H. Hng, F. Boey, T. Zhang and S. Li, *Waste Energy Harvesting*, Springer, London, 2014, vol. 24.
5 S. B. Riffat and X. Ma, *Appl. Therm. Eng.*, 2003, **23**, 913–935.
6 B. M. S. Dresselhaus, G. Chen, M. Y. Tang, R. Yang, H. Lee, D. Wang, Z. Ren and J. Fleurial, *Adv. Mater.*, 2007, **19**, 1043–1053.
7 A. Królicka and M. Michalska, *Phys. B*, 2017, **520**, 89–96.
8 Y. Wang, Y. Sui, H. Fan, X. Wang, Y. Su, W. Su and X. Liu, *Chem. Mater.*, 2009, **21**, 4653–4660.
9 I. Terasaki, Y. Sasago and K. Uchinokura, *Phys. Rev. B: Condens. Matter Mater. Phys.*, 1997, **56**, 685–687.
10 E. V. Mostovshchikova, S. V. Naumov, A. A. Makhnev, N. I. Solin and S. V. Telegin, *J. Exp. Theor. Phys.*, 2014, **118**, 297–303.
11 I. Gil De Muro, M. Insausti, L. Lezama and T. Rojo, *J. Solid State Chem.*, 2005, **178**, 928–936.
12 Y. Yin, B. Tudu and A. Tiwari, *Vacuum*, 2017, **146**, 356–374.
13 B. Zhan, J. Lan, Y. Liu, Y. Lin, Y. Shen and C. Nan, *J. Mater. Sci. Technol.*, 2014, **30**, 821–825.
14 H. Wang and C. Wang, *Mater. Res. Bull.*, 2012, **47**, 2252–2256.
15 A. Kosuga, Y. Isse, Y. Wang, K. Koumoto and R. Funahashi, *Appl. Phys.*, 2009, **105**, 4–9.
16 J. W. Seo, J. Cha, S. O. Won and K. Park, *J. Am. Ceram. Soc.*, 2017, **100**, 3608–3617.
17 T. Yang and T. Cheng, *RSC Adv.*, 2017, **7**, 44659–44664.
18 C. M. Kim, D. H. Kim, H. Y. Hong and K. Park, *J. Eur. Ceram. Soc.*, 2020, **40**, 735–741.
19 T. Liu, J. Chen, M. Li, G. Han, C. Liu, D. Zhou, J. Zou, Z. G. Chen and L. Yang, *Chem. Eng. J.*, 2021, **408**, 127364.
20 A. Vijay, C. P. S, R. Jose, P. Vineetha and K. Venkata Saravanan, *Cryst. Res. Technol.*, 2022, **57**, 2200041.
21 J. Rodríguez-Carvajal, *Phys. B*, 1993, **192**, 55–69.
22 Y. Li, S. Hao, X. Xia, J. Xu, X. Du, S. Fang and X. Meng, *J. Electron. Mater.*, 2013, **42**, 745–751.
23 J. A. Alonso, M. J. Martínez-Lope, M. T. Casais and M. T. Fernández-Díaz, *Inorg. Chem.*, 2000, **39**, 917–923.
24 Y. Wang, Y. Sui, J. Cheng, X. Wang, Z. Lu and W. Su, *J. Phys. Chem. C*, 2009, **113**, 12509–12516.
25 V. Di Castro and G. Polzonetti, *J. Electron Spectrosc. Relat. Phenom.*, 1989, **48**, 117–123.
26 R. Kabir, T. Zhang, R. Donelson, D. Wang, R. Tian, T. T. Tan, B. Gong and S. Li, *Phys. Status Solidi A*, 2014, **211**, 1200–1206.
27 M. C. Biesinger, B. P. Payne, A. P. Grosvenor, L. W. M. Lau, A. R. Gerson and R. S. C. Smart, *Appl. Surf. Sci.*, 2011, **257**, 2717–2730.
28 F. Paquin, J. Rivnay, A. Salleo, N. Stingelin and C. Silva, *J. Mater. Chem. C*, 2015, **3**, 10715–10722.
29 S. H. Estemirova, A. V Fetisov and V. B. Fetisov, *J. Appl. Spectrosc.*, 2009, **76**, 394–401.
30 Y. Wang, Y. Sui and W. Su, *J. Appl. Phys.*, 2008, **104**, 093703.
31 L. Sudheendra, A. R. Raju and C. N. R. Rao, *J. Phys.: Condens. Matter*, 2003, **15**, 895–905.
32 B. Raveau, A. Maignan, C. Martin and M. Hervieu, *Chem. Mater.*, 1998, **10**, 2641–2652.
33 T. Fukui, M. Matsuzawa, R. Funahashi and A. Kosuga, *J. Electron. Mater.*, 2013, **42**, 1548–1553.
34 M. Hossain Khan, S. Pal and E. Bose, *Phys. Scr.*, 2015, **90**, 035803.
35 M. E. M. Jorge, M. Nunes, R. S. Maria and D. Sousa, *Chem. Mater*, 2005, **17**, 2069–2075.
36 D. P. Karim and A. T. Aldred, *Phys. Rev. B: Condens. Matter Mater. Phys.*, 1979, **20**, 2255.
37 S. Jaiswar and K. D. Mandal, *J. Phys. Chem. C*, 2017, **121**, 19586–19601.
38 T. Reimann and J. Töpfer, *J. Alloys Compd.*, 2017, **699**, 788–795.
39 S. Mollah, H. L. Huang, H. D. Yang, S. Pal, S. Taran and B. K. Chaudhuri, *J. Magn. Magn. Mater.*, 2004, **284**, 383–394.
40 R. D. Shannon, *Acta Crystallogr., Sect. A: Cryst. Phys., Diffr., Theor. Gen. Crystallogr.*, 1976, **32**, 751.
41 V. M. Loktev and Y. G. Pogorelov, *Low Temp. Phys.*, 2000, **26**, 171–193.
42 Y. Wang, Y. Sui, X. Wang and W. Su, *J. Phys. D: Appl. Phys.*, 2009, **42**, 055010.
43 R. Ang, Y. P. Sun, Y. Q. Ma, B. C. Zhao, X. B. Zhu and W. H. Song, *J. Appl. Phys.*, 2006, **100**, 063902.
44 N. F. Mott, *Electronic processes in non-crystalline solids*, Oxford, 1971.
45 A. Nag and V. Shubha, *J. Electron. Mater.*, 2014, **43**, 962–977.
46 P. Thiel, S. Populoh, S. Yoon, G. Saucke, K. Rubenis and A. Weidenkaff, *J. Phys. Chem. C*, 2015, **119**, 21860–21867.
47 D. Marsh and P. Parris, *Phys. Rev. B: Condens. Matter Mater. Phys.*, 1996, **54**, 16602–16607.
48 B. Zhan, J. Lan, Y. Liu, Y. Lin, Y. Shen and C. Nan, *J. Mater. Sci. Technol.*, 2014, **30**, 821–825.
49 G. J. Snyder and E. S. Toberer, *Nat. Mater.*, 2008, **7**, 105–114.
50 H. Wang and C. Wang, *Mater. Res. Bull.*, 2012, **47**, 2252–2256.
51 R. Ogawa, S. Fujihara and M. Hagiwara, *J. Ceram. Soc. Japan*, 2022, **130**, 403–409.
52 Y. Zhu, C. Wang, W. Su, J. Liu, J. Li, Y. Du and Y. Li, *Mater. Res. Innov.*, 2014, **18**, S4101–S4105.